# Thermal-Induced Coloration and Photothermal Conversion of an Ag-Based Coordination Polymer with Stable Radicals

Hua Ke,[a] Tong Xie,[a] Jian-Zhen Liao,[a,b*]

[a] College of Materials and Chemical Engineering, Pingxiang University, Pingxiang, Jiangxi 337055 (PR China); E-mail: jianzhenliao@sina.com

[b] State Key Laboratory of Structural Chemistry, Fujian Institute of Research on the Structure of Matter, Chinese Academy of Sciences, Fuzhou, Fujian 350002 (PR China).

**Table of Contents**

## 1. Materials and Physical Measurements

All chemicals were obtained from commercial sources and used as received without further purification. Powder X-ray diffraction (PXRD) analyses were performed on a Bruker D8 Advance diffractometer with Cu Kα radiation ($\lambda$ = 1.5418 Å). Fourier transform infrared (FT-IR) spectra were collected in the range 4000 – 400 $cm^{-1}$ on a PerkinElmer 2000 FT-IR spectrometer with pressed KBr pellets. Optical diffuse reflectance spectra were measured at room temperature on a Shimadzu UV-2600i UV-vis-NIR spectrophotometer. Electron paramagnetic resonance (EPR) spectra were recorded on a Bruker BioSpin E500 EPR spectrometer with a 100 kHz magnetic field modulation at room temperature. Thermal analysis curve was performed on a Mettler Toledo TGA/DSC 1 STAR$^e$ system from room temperature to 800 ℃ with a heating rate of 10 K/min under nitrogen.

## 2. Synthesis of Compound Ag-PTSA

A mixture of 1,3,6,8-pyrenetetrasulfonicacid tetrasodium salt (0.0305 g, 0.05 mmol), $AgNO_3$ (0.0169 g, 0.1 mmol), $H_2O$ (0.5 mL), and MeOH (2.5 mL) were heated in a 25 mL Teflon-lined autoclave at 120 ℃ for 3 days, followed by programmed cooled for 1 day to room temperature. After suction filtration, the faint yellow crystals were collected. Yield: 54% (based on Ag).

## 3. Crystallographic Data Collection and Refinement

A suitable crystal of compound **Ag-PTSA** was selected and collected on a XtaLAB Synergy R, HyPix diffractometer. Using Olex2[S1], the structure was solved with the ShelXS[S2] structure solution program using Direct Methods and refined with the ShelXL[S3] refinement package using Least Squares minimisation. Crystallographic data has been deposited at the Cambridge

Crystallographic Data Center with reference number CCDC 2348216-2348223. These data can be obtained free of charge from The Cambridge Crystallographic Data Centre via https://www.ccdc.cam.ac.uk/structures/.

## 4. Crystal Data for Compound Ag-PTSA

Table S1. Crystal data and structure refinement for **Ag-PTSA** under different temperatures.

| Identification code | Ag-PTSA-100K | Ag-PTSA-150K | Ag-PTSA-200K | Ag-PTSA-250K | Ag-PTSA-300K | Ag-PTSA-350K | Ag-PTSA-400K | Ag-PTSA-450K |
|---|---|---|---|---|---|---|---|---|
| Empirical formula | $C_{16}H_6Ag_3NaO_{12}S_4$ | $C_{16}H_6Ag_3NaO_{12}S_4$ | $C_{16}H_6Ag_3NaO_{12}S_4$ | $C_{16}H_6Ag_3NaO_{12}S_4$ | $C_{16}H_6Ag_3NaO_{12}S_4$ | $C_{16}H_6Ag_3NaO_{12}S_4$ | $C_{16}H_6Ag_3NaO_{12}S_4$ | $C_{16}H_6Ag_3NaO_{12}S_4$ |
| Formula weight | 865.05 | 865.05 | 865.05 | 865.05 | 865.05 | 865.05 | 865.05 | 865.05 |
| Temperature/K | 100.0(1) | 150.0(1) | 200.0(1) | 250.0(1) | 300.0(1) | 350.0(1) | 400.0(1) | 450.0(1) |
| Crystal system | monoclinic | monoclinic | monoclinic | monoclinic | monoclinic | monoclinic | monoclinic | monoclinic |
| Space group | C2/c | C2/c | C2/c | C2/c | C2/c | C2/c | C2/c | C2/c |
| a/Å | 13.50180(18) | 13.52738(17) | 13.54901(18) | 13.56822(19) | 13.59615(20) | 13.62701(18) | 13.6495(3) | 13.6487(7) |
| b/Å | 13.45056(17) | 13.44870(15) | 13.44746(18) | 13.44708(18) | 13.44810(19) | 13.44866(17) | 13.4499(3) | 13.4690(5) |
| c/Å | 11.34272(13) | 11.34736(13) | 11.35488(14) | 11.36442(14) | 11.37621(14) | 11.38885(14) | 11.3903(2) | 11.3969(4) |
| α/° | 90 | 90 | 90 | 90 | 90 | 90 | 90 | 90 |
| β/° | 90.2065(11) | 90.3005(11) | 90.3637(11) | 90.4604(12) | 90.5616(12) | 90.7379(11) | 90.8540(18) | 90.888(4) |
| γ/° | 90 | 90 | 90 | 90 | 90 | 90 | 90 | 90 |
| Volume/Å³ | 2059.90(4) | 2064.35(4) | 2068.82(5) | 2073.41(5) | 2079.96(5) | 2087.01(5) | 2090.84(7) | 2094.88(16) |
| Z | 4 | 4 | 4 | 4 | 4 | 4 | 4 | 4 |
| $\rho_{calc}g/cm^3$ | 2.789 | 2.783 | 2.777 | 2.771 | 2.762 | 2.753 | 2.748 | 2.743 |
| $\mu/mm^{-1}$ | 27.324 | 27.265 | 27.206 | 27.146 | 27.060 | 26.969 | 26.919 | 26.867 |
| F(000) | 1656.0 | 1656.0 | 1656.0 | 1656.0 | 1656.0 | 1656.0 | 1656.0 | 1656.0 |
| Crystal size/mm³ | 0.06 × 0.04 × 0.03 | 0.06 × 0.04 × 0.03 | 0.06 × 0.04 × 0.03 | 0.06 × 0.04 × 0.03 | 0.06 × 0.04 × 0.03 | 0.06 × 0.04 × 0.03 | 0.06 × 0.04 × 0.03 | 0.06 × 0.04 × 0.03 |
| Radiation | Cu Kα (λ = 1.54184) | Cu Kα (λ = 1.54184) | Cu Kα (λ = 1.54184) | Cu Kα (λ = 1.54184) | Cu Kα (λ = 1.54184) | Cu Kα (λ = 1.54184) | Cu Kα (λ = 1.54184) | Cu Kα (λ = 1.54184) |
| 2Θ range for data collection/° | 9.28 to 149.848 | 9.272 to 149.624 | 9.266 to 149.948 | 9.26 to 149.896 | 9.25 to 149.878 | 9.24 to 149.622 | 9.232 to 149.86 | 9.226 to 151.598 |
| Index ranges | -16 ≤ h ≤ 16, -16 ≤ k ≤ 16, -12 ≤ l ≤ 14 | -16 ≤ h ≤ 16, -16 ≤ k ≤ 15, -14 ≤ l ≤ 12 | -16 ≤ h ≤ 16, -16 ≤ k ≤ 16, -11 ≤ l ≤ 14 | -16 ≤ h ≤ 16, -16 ≤ k ≤ 16, -14 ≤ l ≤ 12 | -16 ≤ h ≤ 16, -16 ≤ k ≤ 16, -14 ≤ l ≤ 10 | -16 ≤ h ≤ 17, -16 ≤ k ≤ 16, -14 ≤ l ≤ 12 | -17 ≤ h ≤ 16, -16 ≤ k ≤ 16, -12 ≤ l ≤ 14 | -17 ≤ h ≤ 16, -16 ≤ k ≤ 16, -10 ≤ l ≤ 14 |
| Reflections collected | 10128 | 9024 | 11105 | 10944 | 10956 | 10997 | 11186 | 11174 |
| Independent reflections | 2068 [$R_{int}$ = 0.0319, $R_{sigma}$ = 0.0210] | 2054 [$R_{int}$ = 0.0322, $R_{sigma}$ = 0.0225] | 2077 [$R_{int}$ = 0.0310, $R_{sigma}$ = 0.0186] | 2088 [$R_{int}$ = 0.0310, $R_{sigma}$ = 0.0194] | 2084 [$R_{int}$ = 0.0292, $R_{sigma}$ = 0.0185] | 2100 [$R_{int}$ = 0.0309, $R_{sigma}$ = 0.0207] | 2105 [$R_{int}$ = 0.0309, $R_{sigma}$ = 0.0195] | 2103 [Rint = 0.0835, Rsigma = 0.0542] |

| | | | | | | | | |
|---|---|---|---|---|---|---|---|---|
| Data/restraints/parameters | 2068/0/165 | 2054/0/165 | 2077/0/165 | 2088/0/165 | 2084/0/165 | 2100/0/165 | 2105/1/169 | 2103/0/168 |
| Goodness-of-fit on $F^2$ | 1.043 | 1.063 | 1.056 | 1.047 | 1.058 | 1.071 | 1.102 | 1.039 |
| Final R indexes [I>=2σ (I)] | $R_1$ = 0.0363, wR$_2$ = 0.0970 | $R_1$ = 0.0368, wR$_2$ = 0.1006 | $R_1$ = 0.0386, wR$_2$ = 0.1053 | $R_1$ = 0.0394, wR$_2$ = 0.1079 | $R_1$ = 0.0426, wR$_2$ = 0.1190 | $R_1$ = 0.0472, wR$_2$ = 0.1344 | $R_1$ = 0.0495, wR$_2$ = 0.1442 | R1 = 0.0820, wR2 = 0.2644 |
| Final R indexes [all data] | $R_1$ = 0.0366, wR$_2$ = 0.0972 | $R_1$ = 0.0374, wR$_2$ = 0.1011 | $R_1$ = 0.0392, wR$_2$ = 0.1057 | $R_1$ = 0.0402, wR$_2$ = 0.1086 | $R_1$ = 0.0436, wR$_2$ = 0.1201 | $R_1$ = 0.0484, wR$_2$ = 0.1358 | $R_1$ = 0.0511, wR$_2$ = 0.1459 | R1 = 0.0933, wR2 = 0.3149 |
| Largest diff. peak/hole / e Å$^{-3}$ | 1.79/-2.46 | 1.84/-2.47 | 1.69/-2.47 | 1.54/-2.48 | 1.43/-2.51 | 1.40/-2.70 | 1.68/-2.34 | 2.10/-3.15 |

## 5. Photothermal Conversion Properties Measurement

The 50 mg **Ag-PTSA** original sample (or 400 ℃ heat-treated sample) was pressed into 5-mm-diameter pellets using a manual tablet press at the pressure of 3.75 Mpa. The obtained pellet was under continuous irradiation of a 808 nm laser until the sample reached a steady-state temperature. The temperature was monitored every 10 s by a Fluke (Ti400+) thermal imaging camera. The 808 nm laser beam was irradiated at a power density from 0.4 to 1.6 W cm$^{-2}$.

## 6. Computational Studies

The Vienna Ab-initio Simulation Package (VASP) was employed to conduct all Density Functional Theory (DFT) calculations.[S4-S5] The Perdew-Burke-Ernzerhof (PBE) exchange-correlation functional, employing the generalized gradient approximation (GGA) method with Grimme D3 dispersion correction, was utilized in this study.[S6-S8] The projected augmented wave (PAW) method was utilized to describe core-valence interactions in all DFT calculations.[S9] The energy cutoff for plane wave expansions was set to 550 eV, and the $1 \times 1 \times 1$ Monkhorst-Pack grid k-points were used to sample the Brillouin zone integration for structural optimization. To compute the band structures, open-source package VASPKIT[S10] is applied to generated corresponding k-points with high symmetry and analysis the band structures.
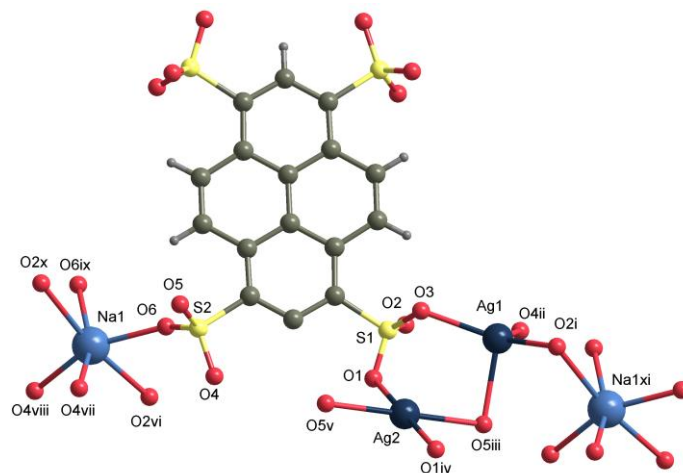
## 7. Related Figures



**Figure S1.** View of the coordination environment of central metal cations in compound **Ag-PTSA**.

Symmetry codes: i) x, 1-y, 0.5+z; ii) 1.5-x, 0.5+y, 1.5-z; iii) 0.5+x, 0.5-y, 0.5+z; iv) 1.5-x, 0.5-y, 2-z; v) 1-x, y, 1.5-z; vi) 1.5-x, 0.5-y, 1-z; vii) 1-x, -y, 1-z; viii) x, -y, -0.5+z; ix) 1-x, y, 0.5-z; x) -0.5+x, 0.5-y, -0.5+z; xi) 0.5+x, 0.5+y, 1+z. Note: The atoms represented by different color in figure: dark turquiose(Na), dark teal blue(Ag), yellow(S), red(O), yellow gray(C), light gray(H).
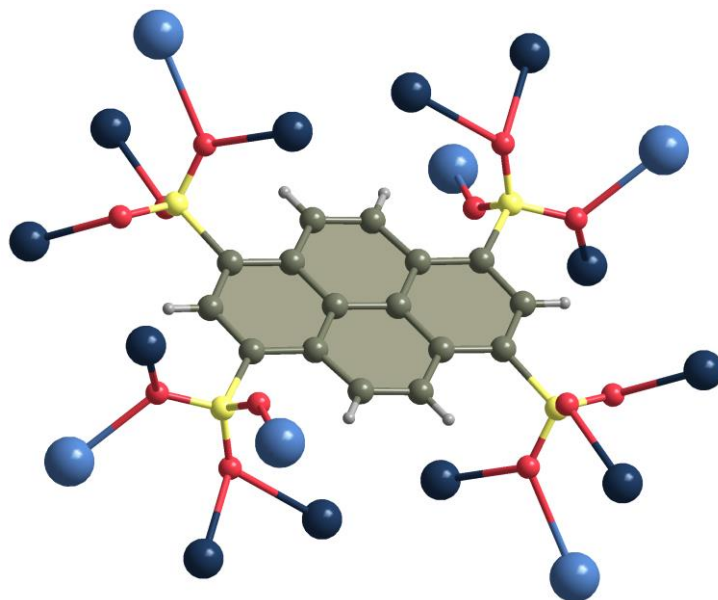


**Figure S2.** Each deprotonated **PTSA** molecule connecting adjacent twelve $Ag^+$ and six $Na^+$ cations in the structure of **Ag-PTSA**. Note: The atoms represented by different color in figure:

dark turquiose(Na), dark teal blue(Ag), yellow(S), red(O), yellow gray(C), light gray(H).
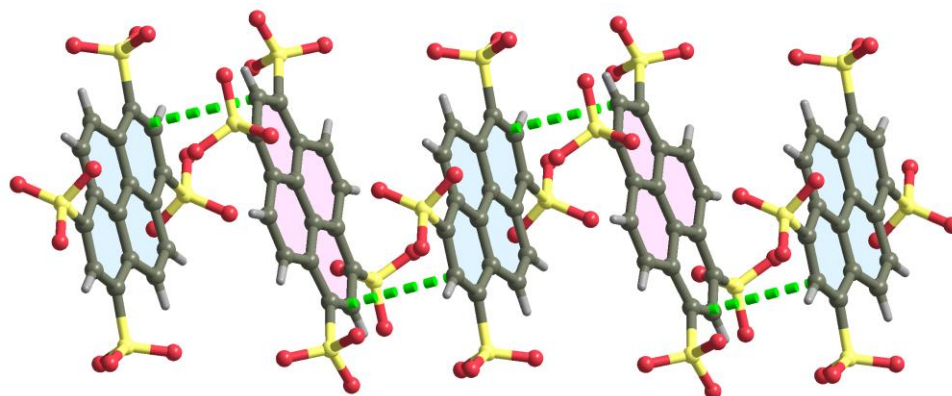


**Figure S3.** The weak π-π interactions between the neighboring ligands in **Ag-PTSA.** Note: The atoms represented by different color in figure: yellow(S), red(O), yellow gray(C), light gray(H).
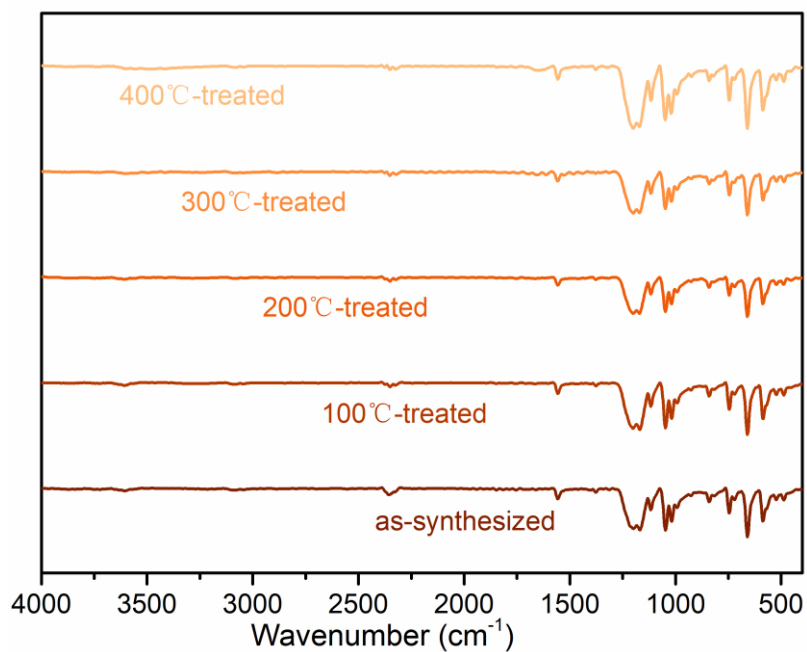


**Figure S4.** The IR spectra of as-synthesized **Ag-PTSA**, and the corresponding heat-treated sample by different temperature.
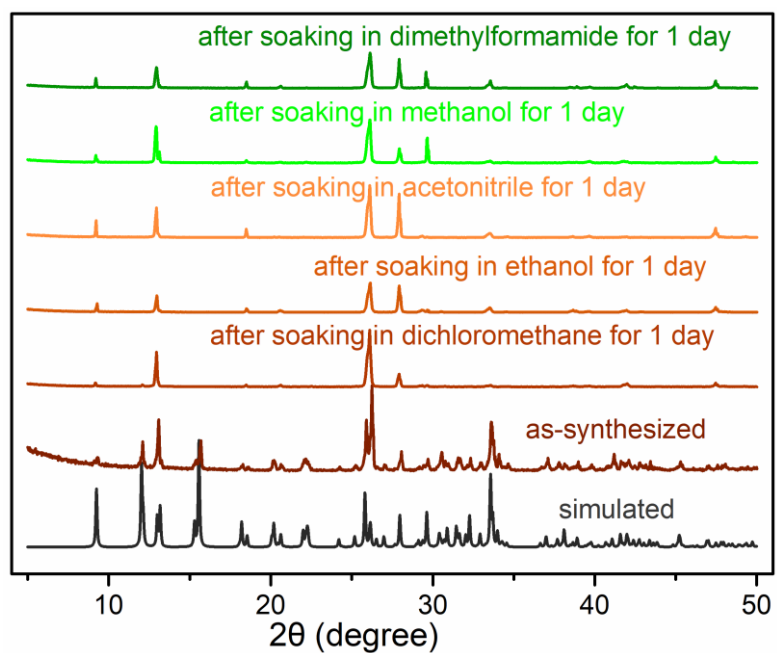
**Figure S5.** The comparison of the X-ray powder diffraction patterns of **Ag-PTSA** crystals after soaking in different organic solvent for 1 day.
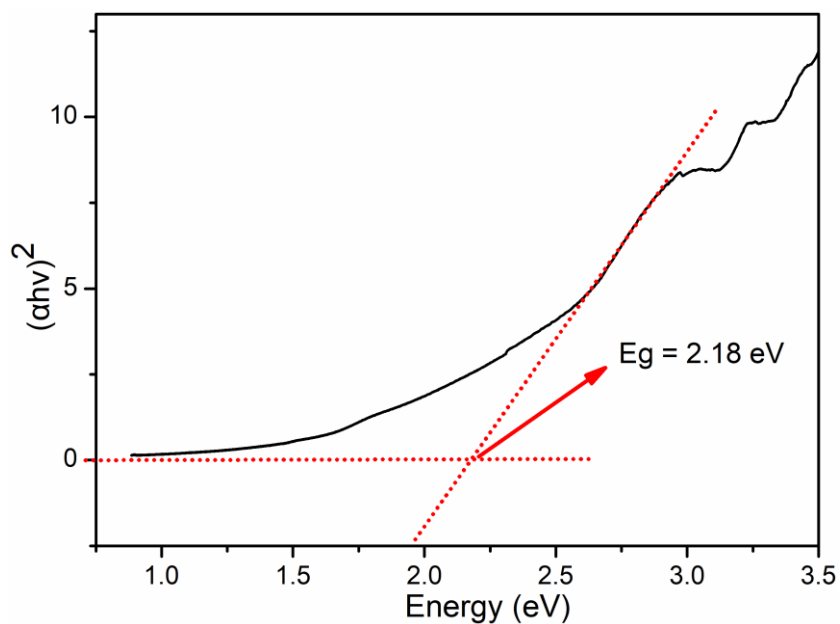


**Figure S6.** The estimated optical bandgap value based on UV-Vis-NIR diffuse reflectance for as-synthesized **Ag-PTSA**.
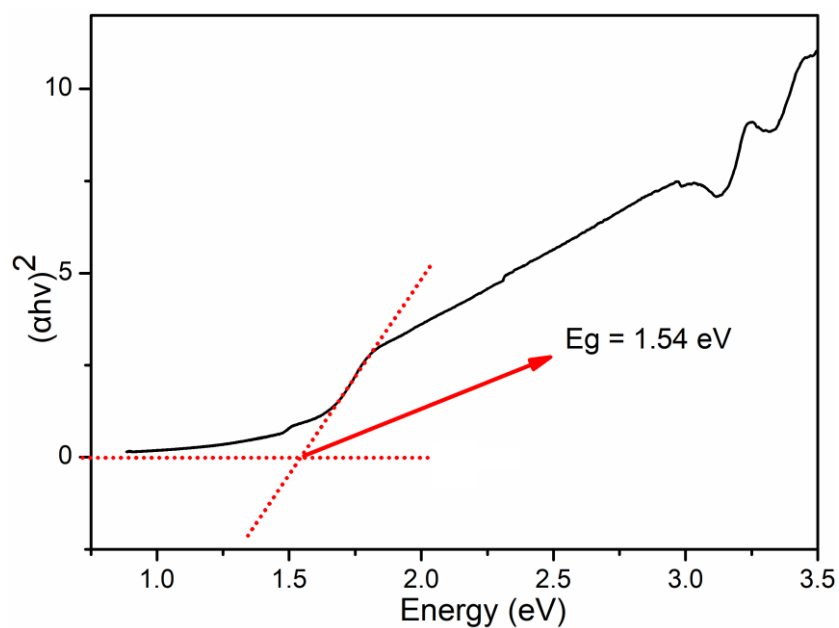
**Figure S7.** The estimated optical bandgap value based on UV-Vis-NIR diffuse reflectance for 400 ℃ heat-treated **Ag-PTSA** sample.
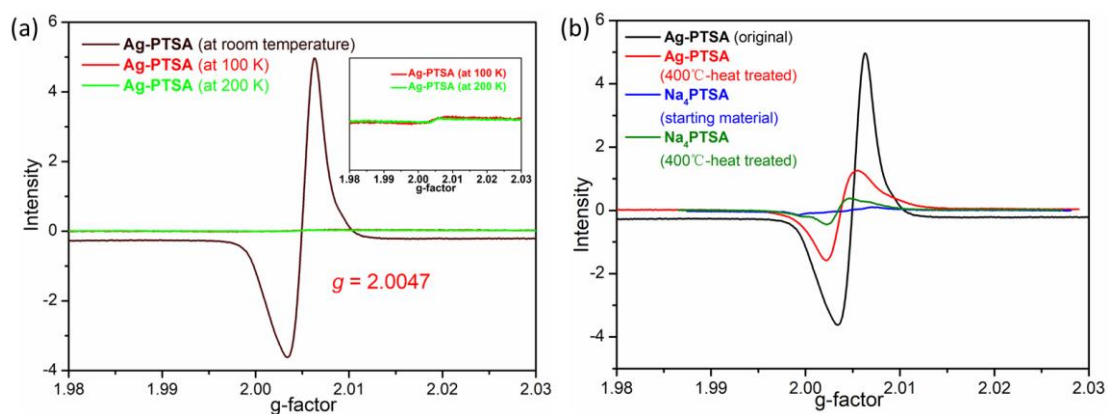


**Figure S8.** (a) The EPR spectra for **Ag-PTSA** crystals at different temperatures; (b) The comparison of the EPR spectra of starting material **Na₄PTSA** powder, **Ag-PTSA** crystals and their corresponding 400℃-heat-treated sample.
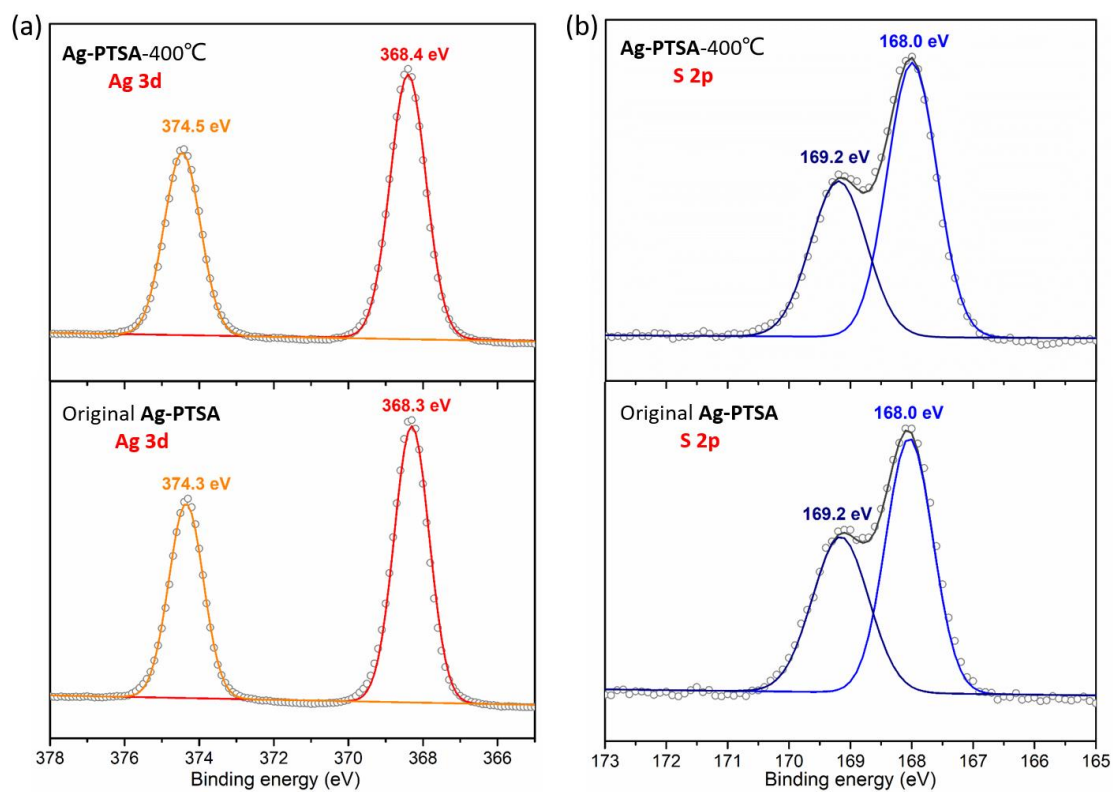
**Figure S9.** (a) The XPS spectra of Ag 3d of **Ag-PTSA** and 400 °C heat-treated **Ag-PTSA**; (b) The

XPS spectra of S 2p of **Ag-PTSA** and 400 °C heat-treated **Ag-PTSA**.
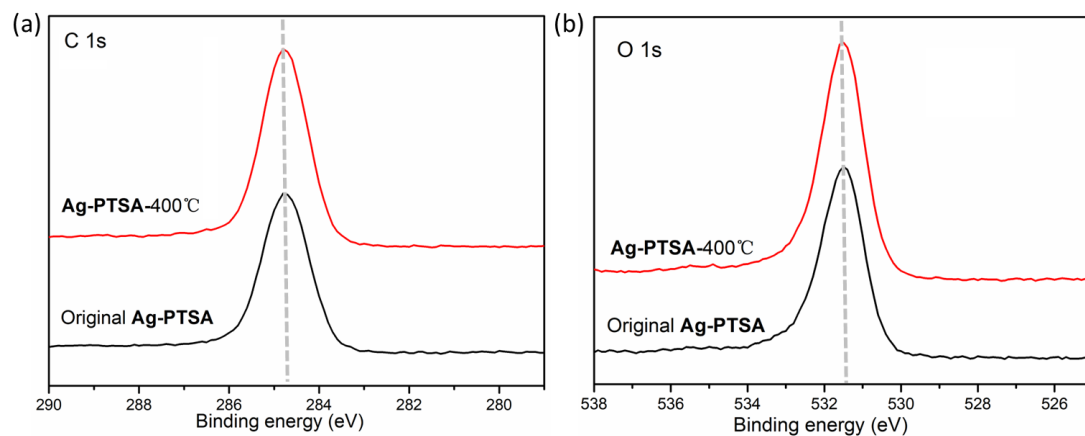


**Figure S10.** (a) The XPS spectra of C 1s of **Ag-PTSA** and 400 °C heat-treated **Ag-PTSA**; (b) The

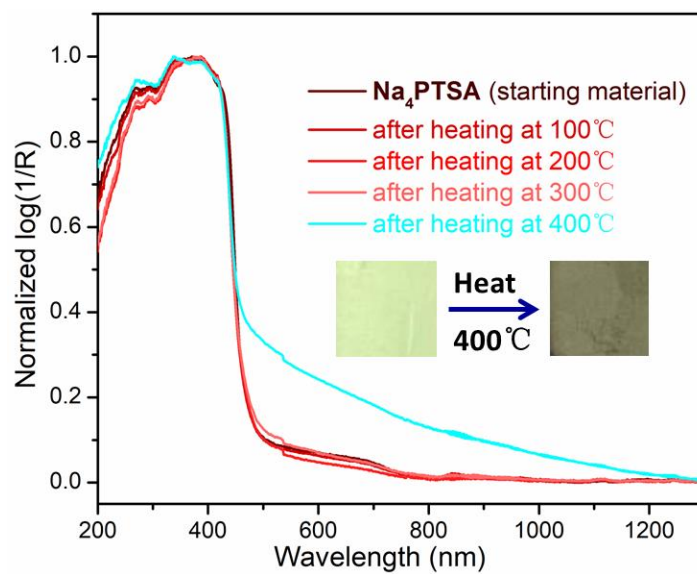XPS spectra of O 1s of **Ag-PTSA** and 400 °C heat-treated **Ag-PTSA**.

**Figure S11.** The changes of the color and UV-vis-NIR spectra of the starting material **Na$_4$PTSA** powder after heating in different temperature.
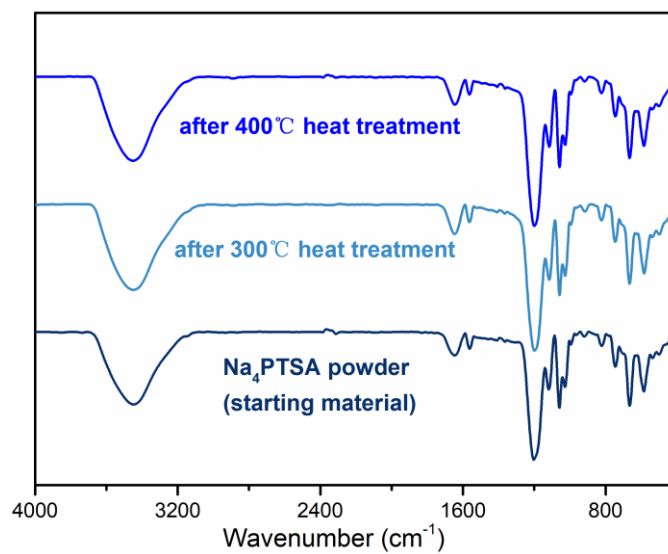


**Figure S12.** The comparison of the IR spectra for the starting material and the corresponding sample that after heating treatment.
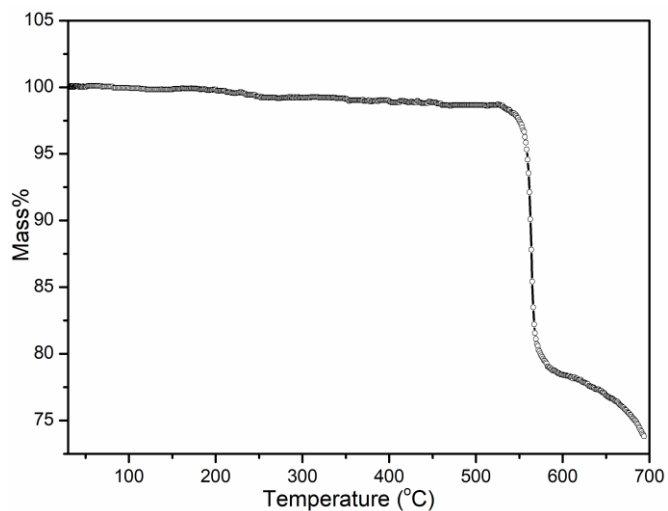
**Figure S13.** The thermogravimetric curve of **Na₄PTSA**.
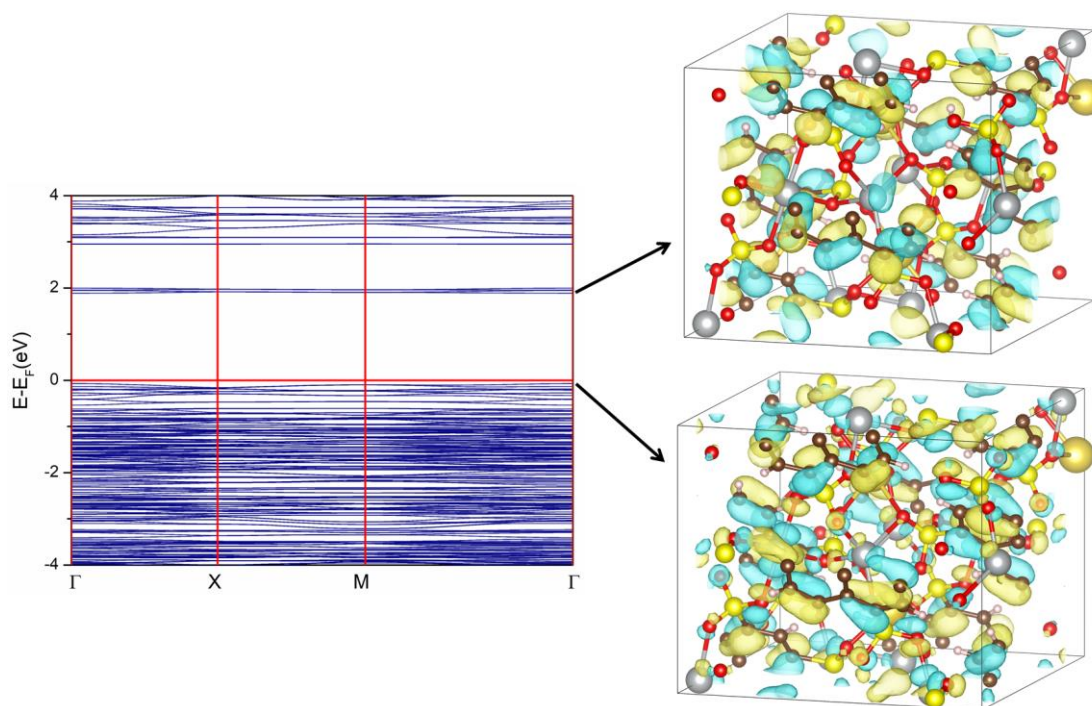


**Figure S14.** The band structure of **Ag-PTSA** (Fermi level located at 0 eV). And the corresponding contributor atoms for the valence band maximum and conduction band minimum of the unit cell of **Ag-PTSA** (the corresponding color of the atoms: metal ion (light gray), carbon (dark brown), oxygen (red); sulphur (yellow), hydrogen (light purplish pink)).
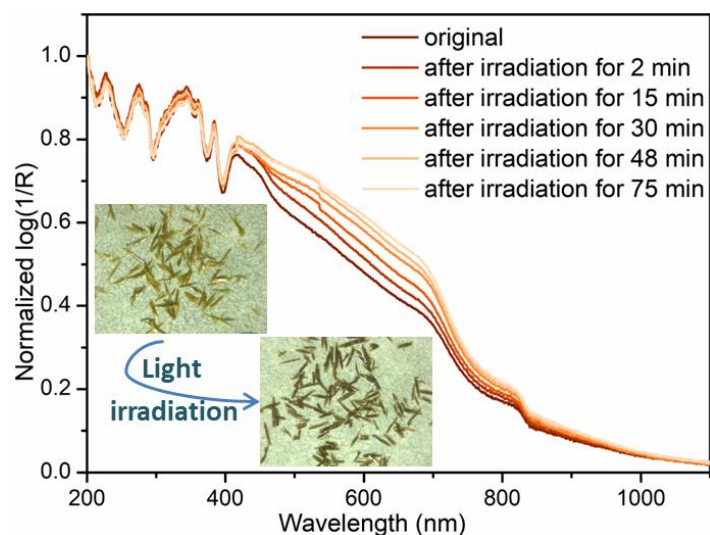
**Figure S15.** In-situ UV-Vis-NIR spectra of **Ag-PTSA** for different irradiation time; the inset picture shows the color changes of **Ag-PTSA** after blue-light irradiation.

To investigate whether additional light exposure causes crystal coloration, the in-situ solid-state UV-vis-NIR spectral changes for **Ag-PTSA** crystals under different light-irradiation time were performed. As shown in Fig. S15, after exposure to blue light ($\lambda$ = 400-460 nm, 3 W) for more than 1 hour, the color of the crystal will be slightly deepened, however, further increasing the irradiation time does not lead to the continuous deepening of color. Notably, it was observed that the absorption within the 420-800 nm band of the UV-vis-NIR spectrum was enhanced as the illumination duration increased, ultimately reaching unchanged, mirroring the observed alteration in crystal color. The color of the irradiated sample does not recover after dark treatment for one week, or even soaked in an ethanol solution with sodium nitrite (which can be acted as both an oxidizing and reducing agent), suggesting its irreversible photo-induced color variation behavior.

The EPR signal intensity of the irradiated sample also decreases compared to the original, which is consistent with the result of heat-induced changes. That is, the crystal appears darker in color, with enhanced UV-vis absorption, yet the EPR signal is reduced, as shown in Fig. S16. After heating or light exposure, the color of the crystal deepens and the absorption intensifies,

while the radicals change color, further demonstrating that in this particular hybrid crystalline material, the process involves not only charge transfer, but also thermal- or photo-induced electron transitions of inorganic-organic hybrid crystalline material.
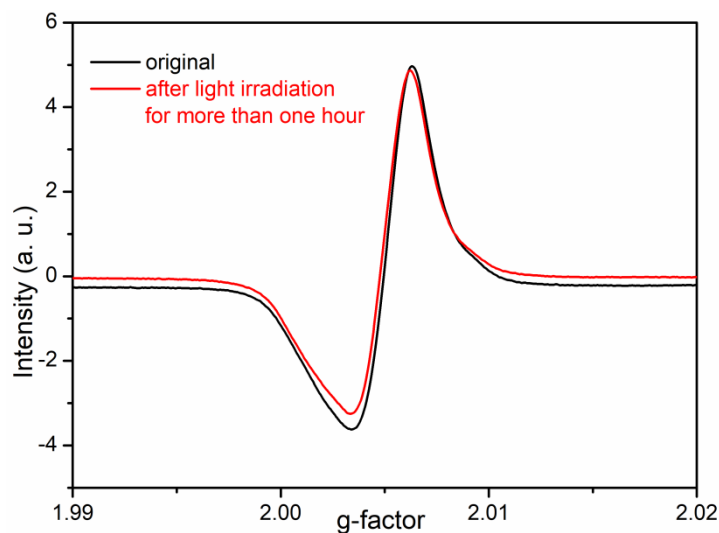


**Figure S16.** The EPR spectra for the **Ag-PTSA** crystal before and after additional light irradiation.
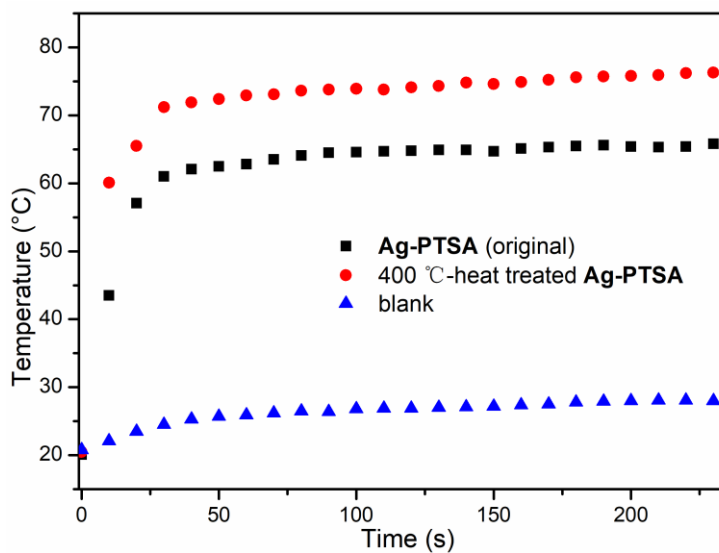


**Figure S17.** The temperature rises of **Ag-PTSA**, its 400 °C-heat treated sample and blank under 808 nm laser irradiation (0.8 W cm$^{-2}$) for different time.
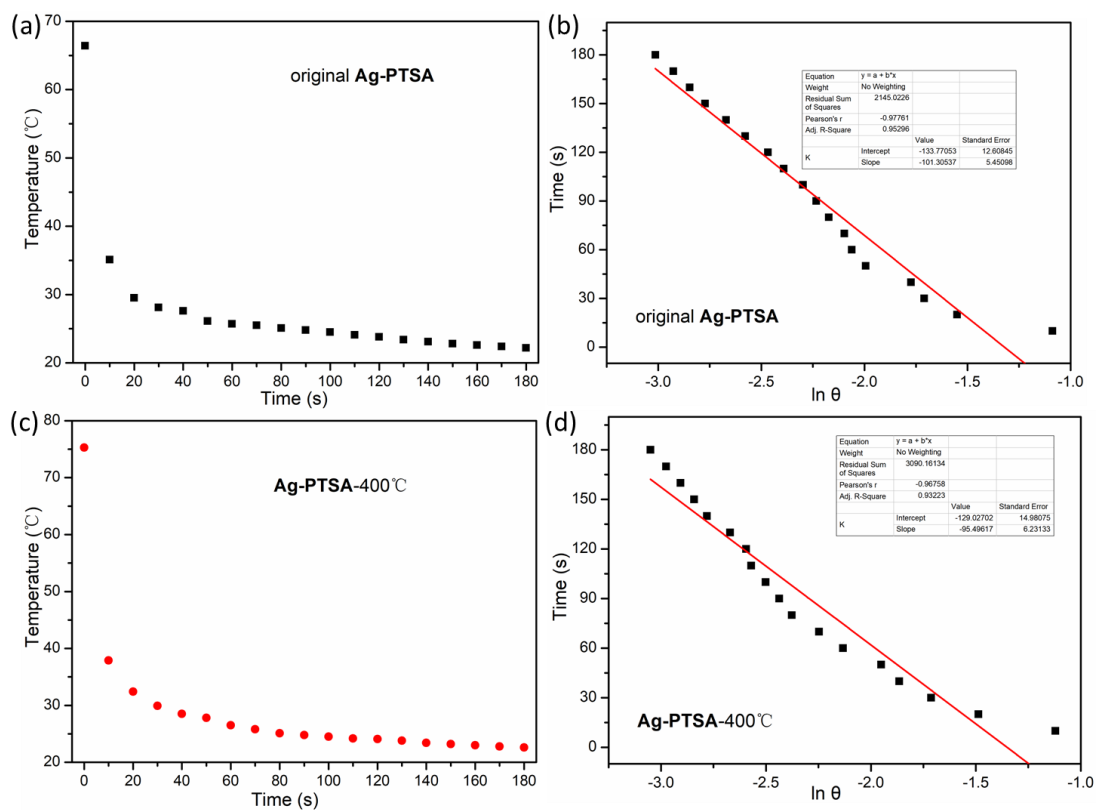
**Figure S18.** (a) The cooling curve of original **Ag-PTSA** after irradiation with 808 nm laser (0.8 W·cm$^{-2}$) and its corresponding time-ln θ linear curve (b). (c) The cooling curve of 400 ℃ heat-treated **Ag-PTSA** after irradiation with 808 nm laser (0.8 W·cm$^{-2}$) and its corresponding time-ln θ linear curve (d).



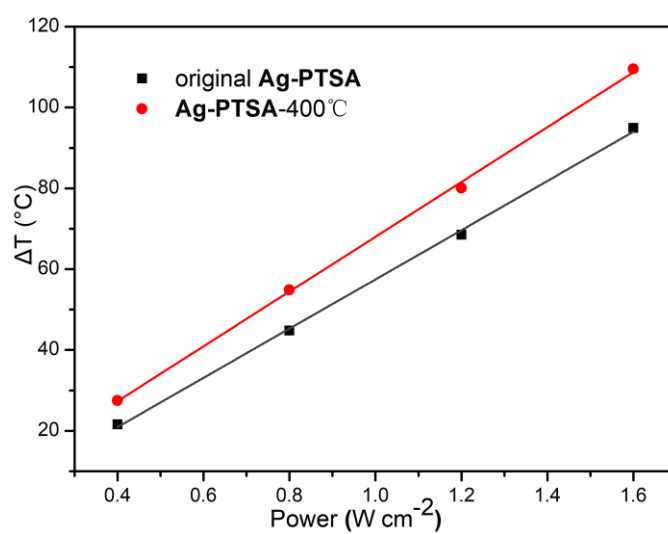**Figure S19.** Average △T as a function of NIR laser intensity (ranging from 0.4 to 1.6 W cm$^{-2}$).

## 8. Reference

S1 O.V. Dolomanov, L.J. Bourhis, R.J. Gildea, J.A.K. Howard, H. Puschmann, OLEX2: A Complete Structure Solution, Refinement and Analysis Program, *J. Appl. Cryst.,* 2009, **42**, 339-341.

S2 L.J. Bourhis, O.V. Dolomanov, R.J. Gildea, J.A.K. Howard, H. Puschmann, The anatomy of a comprehensive constrained, restrained refinement program for the modern computing environment - Olex2 dissected, *Acta Cryst.,* 2015, **A71**, 59-75.

S3 G.M. Sheldrick, SHELXT-Integrated space-group and crystal-structure determination, *Acta Cryst.*, 2015, **C71**, 3-8.

S4 G. Kresse, J. Hafner, Ab Initiomolecular Dynamics for Liquid Metals, *Phys. Rev. B,* 1993, **47**, 558-561.

S5 G. Kresse, J. Hafner, Ab Initiomolecular-Dynamics Simulation of the Liquid-Metal-Amorphous-Semiconductor Transition in Germanium, *Phys. Rev. B,* 1994, **49**, 14251-14269.

S6 J. P. Perdew, K. Burke, M. Ernzerhof, Generalized Gradient Approximation Made Simple. *Phys. Rev. Lett.,* 1996, **77**, 3865-3868.

S7 G. Kresse, D. Joubert, From Ultrasoft Pseudopotentials to the Projector Augmented-Wave Method. *Phys. Rev. B,* 1999, **59**, 1758-1775.

S8 J. Moellmann, S. Grimme, DFT-D3 study of some molecular crystals. *J. Phys. Chem. C*, 2014, **118**, 14, 7615-7621.

S9 P. E. Blöchl, Projector Augmented-Wave Method. *Phys. Rev. B,* 1994, **50**, 17953-17979.

S10 V. Wang, N. Xu, J.-C. Liu, G. Tang, W.-T. Geng, VASPKIT: A user-friendly interface

facilitating high-throughput computing and analysis using VASP code. *Comput. Phys. Commun.,* 2021, **267**, 108033.